Large Area Uniaxial-oriented Growth of Freestanding Thin Films at the Liquid-Air Interface with Millimeter-sized Grains

Weiguang Zhu[1], Yanming Zhang[2], Junhua Shen[2], Yunfeng Shi[2], Mingxin Li[1], Jie Lian[1,2,*]

[1] Department of Mechanical, Aerospace and Nuclear Engineering, Rensselaer Polytechnic Institute, Troy, NY 12180, USA

[2] Department of Materials Science and Engineering, Rensselaer Polytechnic Institute, Troy, NY 12180, USA

ABSTRACT: Manipulating materials at the atomic scale and assembling them into macroscopic structures with controlled dimensionalities and single crystal quality are grand scientific challenges. Here, we report a general solvent evaporation method to synthesize large area uniaxial-oriented growth of free-standing thin films at the liquid-air interface. Crystals nucleate at the solution surface and rotate into the same orientation under electrostatic interaction, and then merge as large crystals and grow laterally into a large area uniform thin film with negligible grain boundaries. The lateral dimension is confined only by the size of containers. The film thickness can be tuned by adjusting solvent evaporation rate (R) and solute diffusivity (D), and a characteristic length, $L^* \sim D/R$, is derived to estimate the film thickness. Molecular dynamic (MD) simulations reveal a concentration spike at the liquid-air interface during fast solvent evaporation, leading to the lateral growth of thin films. The large area single crystal-quality films are demonstrated on both inorganic metal halides and hybrid metal halide perovskites. The solvent evaporation approach and the determination of key parameters enabling film thickness prediction pave the way to mass production of thin film materials under controlled evaporation conditions.

KEYWORDS: ***large area-oriented growth, single-crystal quality, liquid-air interface, solvent evaporation, solute diffusivity***

High performance of optoelectronic devices relies on the crystallinity of semiconductor materials.[1] Single crystal metal halide perovskite materials, which have been extensively studied in recent years, possess high light absorption coefficient, large ambipolar mobility, and long charge carrier lifetime.[2-5] However, the majority of current perovskite-based devices are fabricated on polycrystalline thin films, suffering orders magnitude of loss in charge transport characteristics[4,5] and increased tendency of degradation[6,7] due to the high density of grain boundaries. High-throughput methods are required to fabricate large-area and high-quality perovskite thin films to further enable their ultimate practical applications. Solution-based methods are recognized as more cost-effective routes compared to the vacuum-related techniques.[8-10] To achieve scalable production, several methods have been reported, such as spray coating,[11,12] doctor blade coating[13] and slot-die coating.[14] However, these methods can only produce polycrystalline films and still suffer from the challenge to

produce large scale uniform thin films with appropriate compositions for high performance optoelectronics.

Indeed, single-crystalline films of perovskite materials could be obtained using a space-controlled method,[15-18] and the film thickness could be downsized to micrometers. However, the lateral size of the obtained films is usually less than 1 cm due to the difficulty of ion diffusion in the limited micrometer size channel. Solution surface growth of perovskite single crystalline thin films has also been demonstrated previously with limited lateral sizes around 1 cm.[19-21] Kinetically, it is very challenging to suppress the nucleation rate to a very low level, in order to grow large area single crystal thin films, and the competition between nucleation rate and grain growth rate typically results in the growth of polycrystalline films with a 3D island growth mechanism.

Success has been attempted to assemble 2D materials (*e.g.* graphene,[22] hBN[23,24] and MoS_2[25]) into singe crystal films from multiple domains with the same orientation which could be self-aligned and assembled into more energetically favorable single crystal films without grain boundaries. Half-meter-size single crystal graphene was realized via seamless stitching of thousands of unidirectionally-aligned graphene domains by choosing a substrate with same surface symmetry.[26] Without a solid substrate, liquid surface has been previously adopted as a 2D template for thin film growth in a controlled manner.[23, 27-30] For example, h-BN grains could be grown on the liquid Au surface due to the limited solubility of B and N atoms in the liquid Au. The electrostatic interaction between N and B atoms at the edge of different grains with the same orientation rotates and seamlessly stitches them into a wafer-scale single crystal hBN thin film eventually.[23] However, it is still a challenge to control domain orientation and suppress grain boundary formation in solution-based methods, and this concept has not been demonstrated/realized to achieve a large area oriented growth of single crystal metal halide and hybrid halide perovskite films. The precise control and manipulation of materials at the atomic scale and assembly at the macroscopic scale into large-area and single crystal quality films remains a grand material synthesis challenge. Underlying physics and mechanisms governing the competing kinetics of nucleation and grain growth must be revealed in order to advance materials synthesis science to fabricate large-area single crystal films in a controllable and predictable manner.

Here, we report a general solution-based synthesis method for the uniaxial orientation growth of large-area free-standing thin films with millimeter sized grains at the liquid-air interface in minutes by directly evaporating solvent. During fast solvent evaporation, multiple grains nucleate and coalesce on the solution surface, and grow laterally as compact structures until fully coverage. As a result, the lateral dimension of 2D single crystal quality films is only confined by the dimension of container. The scalable solvent evaporation approach at the liquid-air interface represents a potentially high throughput method in manufacturing large-area single crystal quality films. This method is universal and can be applied for a wide range of metal halides and hybrid perovskite materials (*e.g.* PbI_2, BiI_3, $MAPbI_3$, $MAPbBr_3$ and 2D perovskites). Molecular dynamic simulations at the atomic scale elucidate the dominant factors governing nucleation and growth of 2D films based on the spikes of super-saturation of reactants at the liquid-air-interface during fast solvent evaporation. A simple analytical model is developed to discover a characteristic length

($L^* \sim {}^{D}/_{R}$) that can correlate with film thickness and diffusivity of solutes (D)/evaporation rate of solvent (R), enabling a science-based prediction of 2D materials into large-area single crystalline thin films with control film thicknesses. As a result of the substrate free process, the large-area and uniaxial oritented films at the liquid-air interface can be easily transfered and incoroprated for scalable fabrication of devices for functional applications such as solar cells, photodetectors, sensors and x-ray detectors, *etc.*

RESULTS AND DISCUSSION

Based on the classical nucleation theory,[27,28] the driving force for nucleation is supersaturation (σ) which can be quantified in terms of the concentration of solute (c) and the equilibrium concentration (c_e), $\sigma = \ln(c/c_e)$.[27] Thus, the tendency to nucleate becomes higher as the supersaturation increases. As the solution is heated at the bottom, solvent evaporates continuously. Under the assumption that the evaporation rate is very low, solute diffusion is sufficient such that there is no concentration gradient. On the other hand, a high evaporation rate will cause a rapid descend of the liquid-air interface and create a thermal gradient between the surface and the bottom of the solution while solvent evaporates. Due to the limited diffusivity of the solute, it could significantly increase the concertation near the liquid interface and create a concentration spike at the interface. This high concentration gradient will result in higher supersaturation and be more favorable for nucleation and growth along the liquid-air interface (Figure 1A). Our observation implies that two key factors are required for the solution-based surface nucleation and 2D growth: (i) solute diffusivity, which is related to temperature and solvent conditions, (ii) evaporation rate of solvents, to establish concentration spike at the interface. Under well-controlled solute diffusivity and evaporation rate of solvents, wafer-scale single crystalline thin films could be obtained at the liquid-air interface and the film thickness can also be well-tuned.

We chose PbI_2 as a model material partly because PbI_2 films have found many applications, such as in nonlinear optics,[29] luminescence,[30] X-ray/gamma ray detection,[31-33] photodetectors,[34] and as an important raw material for the synthesis of lead-halide perovskites.[39, 40] To obtain PbI_2 thin film, a well-controlled solvent conditions and evaporation rate are desirable. As shown in Figures S1A-E, only particles or PbI2 wires could be obtained under an ethylene glycol environment. Changing the solvent to glycerol with extra air flow over solution surface, thin film could be formed at the solution surface (Figures S1F and G). Thus, the higher viscosity of glycerol ($\eta_{glycerol}$=1.68 mPa·s *vs.* η_{EG}= 0.7 mPa·s, at 200 °C) and the constant air flow are essential and effective for PbI_2 nucleation and growth at the liquid-air interface. In a typical process, PbI_2 solution (50 mg/mL in DMF) was added in a petri dish with 5 mL of glycerol and evaporated on a hot plate (see in experimental method). A fully surface covered PbI_2 thin film with good transparency could be obtained (Figure 1B) and the free-standing PbI_2 thin film also displays good flexibility, shown in Figure 1C. Figure 1D and S2 show the snapshots of PbI_2 thin film nucleation and growth process at the liquid-air interface. As solvent evaporating, yellow PbI_2 small crystals nucleate at the liquid-air interface and tend to rotate into same orientation under the electrostatic interaction and merge together into large-sized

2D crystals, which could be driven by the thermodynamic-driven minimization of the overall energy of the structure (Figure S2). As shown in Figures S2D and 2E, two triangular grains rotate and align into the same orientation, then coalesce together and grow in a large crystal. During the coalescence process, the in-plane strain can induce a continuous rearrangement of PbI_2 lattice at the grain boundary to decrease the orientation dependent energy (Figure S3). Then, these islands grow laterally along the solution surface to form a continuous and uniform thin film across the entire liquid-air interface (Figure 1D and Movie S1). The optical image of the PbI_2 thin film etched by ethylene glycol, displays multiple well-aligned triangular etching pits, suggesting the uniform orientation of the whole thin film (Figure S4).

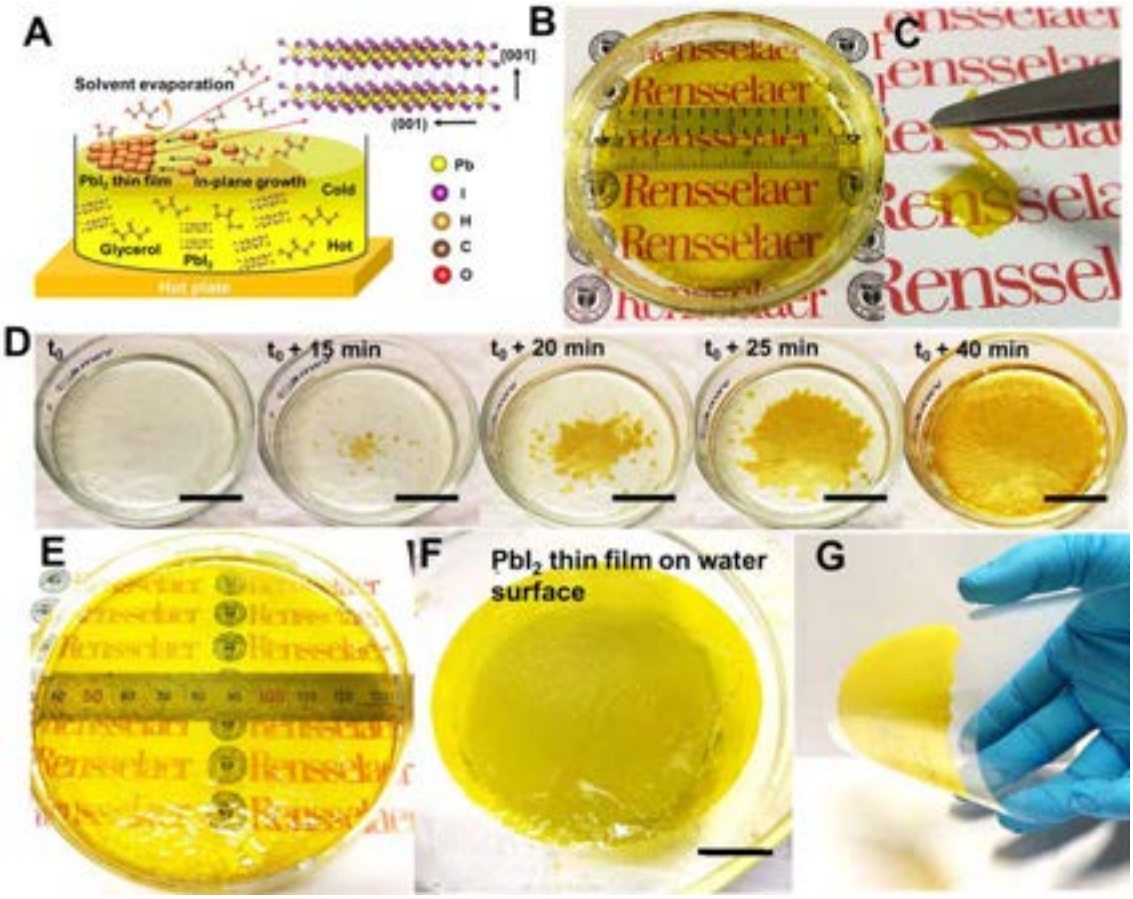

Figure 1. A solution-based wafer-scale growth of PbI_2 thin films at the liquid-air interface: (**A**) A schematic concept of thin film nucleation and growth at the liquid-air interface by solvent evaporation; (B) Optical images of a PbI_2 thin film in 60 mm diameter prepared on the solution surface; (**C**) A free-standing PbI_2 thin film with good flexibility; (**D**) Snapshots of PbI_2 thin film nucleation and growth at the solution surface in a Φ 60 mm petri dish; (**E**) An optical image of a larger sized PbI_2 thin film (Φ 100 mm) only by increasing the size of petri dish; (**F**) An optical image of the prepared PbI_2 thin film which can be floated on water surface for transferring to targeted substrates; (**G**) A large PbI_2 thin film transferred on the PET substrate by a lift-off method, showing good flexibility. Scale bars: 2 cm.

By increasing evaporation rate, the growth of large-area single crystalline quality PbI_2 thin films can be completed very rapidly within 15 mins (Figure S5), demonstrating a potentially high-throughput approach for fabricating wafer scale free-standing thin films. Due to the simplicity of the method, it can be easily enlarged to fabricate much larger-sized thin films by simply increasing the size of container, and therefore, the lateral dimension of the thin films is essentially unlimited. As shown in Figure 1E, over 100 mm in diameter of PbI_2 thin films could be obtained by evaporating solvent at 200 °C, which is the largest area that ever reported on this material. The good transparency indicates high crystallinity of the thin film. In addition, the obtained thin film floats freely on the water surface (Figure 1F), allowing an easy transfer to any targeted substrates. As a demonstration, PbI_2 thin film

can be directly transferred from water to a PET substrate by a lift-off method (Figure 1G). The film displays a good flexibility, which can be integrated into flexible electronics.

The crystalline quality can be further confirmed by X-ray diffraction (XRD) and pole figure measurements. The XRD diffraction peaks of the PbI_2 thin film are very sharp, indicating the film possesses high crystallinity, as shown in Figure 2A. The diffraction peaks located at $2\theta = 12.68^{o}$, 25.49^{o}, 38.62^{o}, and 52.33^{o}, correspond to the (001), (002), (003) and (004) planes of PbI_2, respectively. It is consistent with the reported results for PbI_2 single crystals[35,36] and suggests that the large area PbI_2 thin film is highly oriented parallel to the (001) plane (Figure 2B). The highly oriented thin film is further demonstrated by the sharp rocking curve of (001) diffraction peak with full width at half-maximum (FWHM) of 0.46^{o}. Considering the limited X-ray beam size, XRD diffractions acquired from multi-positions from six different locations (see Figure S6) show almost identical results (Figure S6A). In addition, almost constant FWHMs of the (001) diffraction peaks with only around 0.06° are identified (Figure S6B), indicating the single crystalline quality of the obtained PbI_2 film. Figure 2C shows the $\{10\bar{1}1\}$ pole figure of PbI_2, with 3 sets of six distinct poles $\Delta\varphi = 60°$, which fits well with three single-crystal domains of (001)-oriented hexagonal PbI_2 from the wafer-scale film. As marked by the coordinates, the in-plane orientation of [111] and [101] can also be determined. A SEM-based electron backscatter diffraction (EBSD) was also conducted to inspect the phase purity and the quality. In the experiment, a focused electron beam strikes on the sample surface at an angle of 70°. The diffraction patterns (Kikuchi patterns) were obtained at different positions which show almost identical patterns, indicating no grain boundary within the measure area (Figures S7A-F). The inverse pole figure (IPF) mappings were performed at an area of 1.06×0.60 mm^2 on the film. The homogenous color on the IPF mappings indicate the same crystallographic orientation (Figures S7G-I). The uniform color in the IPF Z mapping (Figure S7H), normal to the sample surface, implying that the crystallites are very well oriented with the {001} planes, parallel to the substrate, in line with the results from XRD and pole figure measurements. Furthermore, the typical scanning electron microscopy (SEM) images of the top surface and cross section of the obtained film are shown in Figures 2D and E. The flat surface in millimeter scale is obviously observed without visible grain boundaries, further confirming the high quality of the fabricated thin film (Figure 2D). It indicates that grains formed at the solution surface could be stitched seamlessly without grain boundaries. The evident layered feature could also be identified from the cross-section SEM, suggesting a layer-by-layer growth nature (Figure 2E). In addition, the prolonged growth after fully surface coverage, screw dislocation growth (Figure S8) can be observed on the surface of PbI_2 thin film due to the lower supersaturation condition.

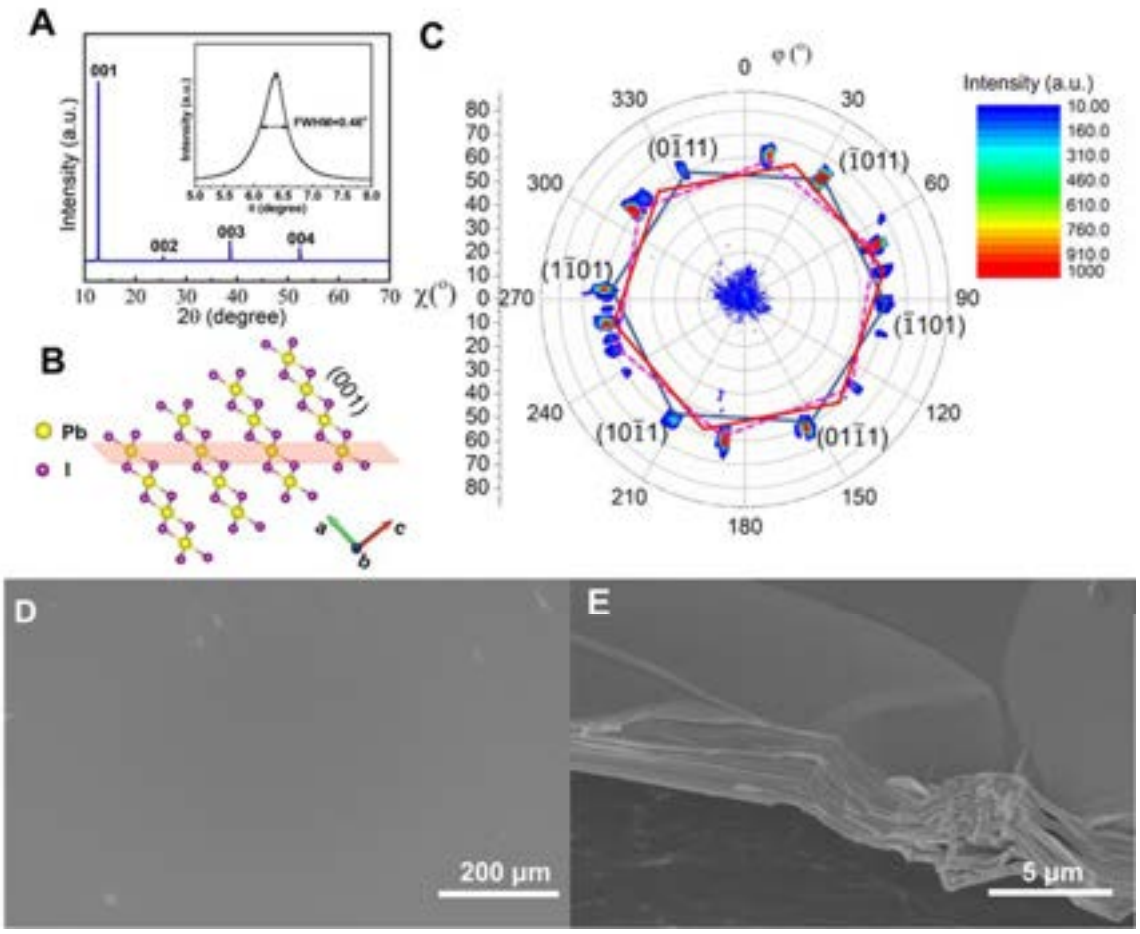

Figure 2. Structural and morphological characterization of PbI_2 thin films showing its essential single crystal quality. (**A**) XRD pattern of the wafer scale PbI_2 thin film recorded by Cu Kα radiation. The insert is the rocking curve measured of the (001) diffraction peak. (**B**) Crystal structure of PbI_2 with a view from [0$\bar{1}$0] direction. The 2D layers are the (001) planes. The pink plane represents the (101) plane. (**C**) {10$\bar{1}$1} pole figure of PbI_2 thin film on a glass substrate. SEM images of surface (**D**) and cross-section (**E**) of PbI_2 thin films.

The absorption spectrum of the PbI_2 thin film exhibits a sharp absorption edge at 522 nm (Figure S9A). Band gap extracted from the Tauc plot shows a value of 2.39 eV, which is in good agreement with the values for the single crystals reported previously.[35,37] The photoluminescence (PL) peak position of PbI_2 film is located at 525 nm (Figure S9B), matching the value reported for the PbI_2 single crystal film synthesized using a temperature gradient method.[35] Photoluminescence measurements of PbI_2 film at different temperature were conducted. As shown in Figure S10A, PL spectra of PbI_2 film were continuously blue-shifted with the decrease in temperature from 298 K to 78 K. The temperature dependence of energy bandgap is a consequence of contributions from electron-phonon interaction and the thermal expansion of the lattice. As the temperature increases, the band gap becomes smaller than that of low temperature due to the enhanced electron-phonon interaction caused by increased phonon population and weak contribution of thermal expansion.[38] The FWHM of PL peak is displayed in Figure S10B. As the temperature

increases, the PL line width broadening is observed. Based on a linear fitting of FWHM values, the broadening of PL emission could be resulted from the acoustic phonon scattering.[39] In addition, at temperature of 78 K, multi-PL peaks were observed (Figure S10C). The line with a peak position at 2.49 eV (FX) is attributed to free excitons, while the line with a peak position at 2.45 eV (BX) is from the bound excitons. The peak position at 2.43 eV (ST) could be attributed to the phonon-assisted shallow level trap state emission. A small peak at 2.39 eV (e-h) can be assigned as donor-acceptor pair emission. The well resolved peaks of PL also suggests the single crystal quality of PbI_2 film. Figure S10D shows the time resolved photoluminescence (TRPL) at different temperatures. The TRPL can be fitted by a biexponential decay behavior. At room temperature, the fast decay (τ_1= 0.082 ns) refers to the free exciton combination and the slow decay (τ_2= 0.34 ns) is attributed to the trapped exciton recombination, which is consistent with the results reported on PbI_2 single crystals[40]. Because of the free-standing configuration, the high quality PbI_2 thin film can be easily transferred on plastic substrates and exhibits excellent flexibility. Figure S11 shows XRD patterns after different bending cycles. Full-width at half-maximum (FWHM) of (001) planes at different bending cycles are less than 0.1°, showing the single crystalline quality of PbI_2 film even after 200 bending cycles (Figure S11C). Thus, it is suitable for the fabrication of flexible optoelectronics.

A prototype flexible photodetector on a PET substrate (Figure S12A) is fabricated with a lateral metal-semiconductor-metal configuration. As the light illumination (405 nm, 2 mW/cm^2) is on, a rapid increased photocurrent can be observed (Figures 3A-C). With a 5 V bias, the on/off ratio reaches as high as 1.7×10^3 and a low dark current of 7 pA was obtained when the light is in the "off" state (Figure 3A). The low dark current indicates a low noise and a high sensitivity, essential for the practical application. As shown in Figure S9B, with the increase of illumination power, the photodetector manifests a good linear relationship with photocurrent. The excellent property/performance of the fabricated PbI_2 flexible photodetector is one of highest responsivities among PbI_2 prepared using different methods (Figure S13) and highly comparable with the results obtained on PbI_2 single crystals in the literature (Supplementary Table S2). This indicates the single crystal quality of PbI_2 thin films obtained at the liquid-air interface through the solvent evaporation-controlled approach. The uniformity of photocurrent measured on 20 devices on the same PbI_2 thin film is further evaluated as shown in Figure 3D, displaying good uniform photo-electronic performance across the substrate. In addition, the mechanical stability after different bending cycles is conducted. The typical bending angle is around 45°. It can be seen that the photocurrent still remains the same order with only a minor reduction after 400 bending cycles, demonstrating excellent mechanical stability of the fabricated PbI_2 flexible photodetector (Figures 3E and F). In addition, compared to the previous reported PbI_2 single crystal film, the lateral size typically lies in a range of millimeters, see in Supplementary Table S3. The PbI_2 thin films synthesized by this solvent evaporation method, not only display a comparable or higher performance than the single crystal based PbI_2 photodetectors, but also have a >10 cm in diameter large size and can be enlarged by increasing the container size. Therefore, this method provides a robust solution to have

potentially high throughput thin film fabrication while having single crystalline level optoelectronic performance.

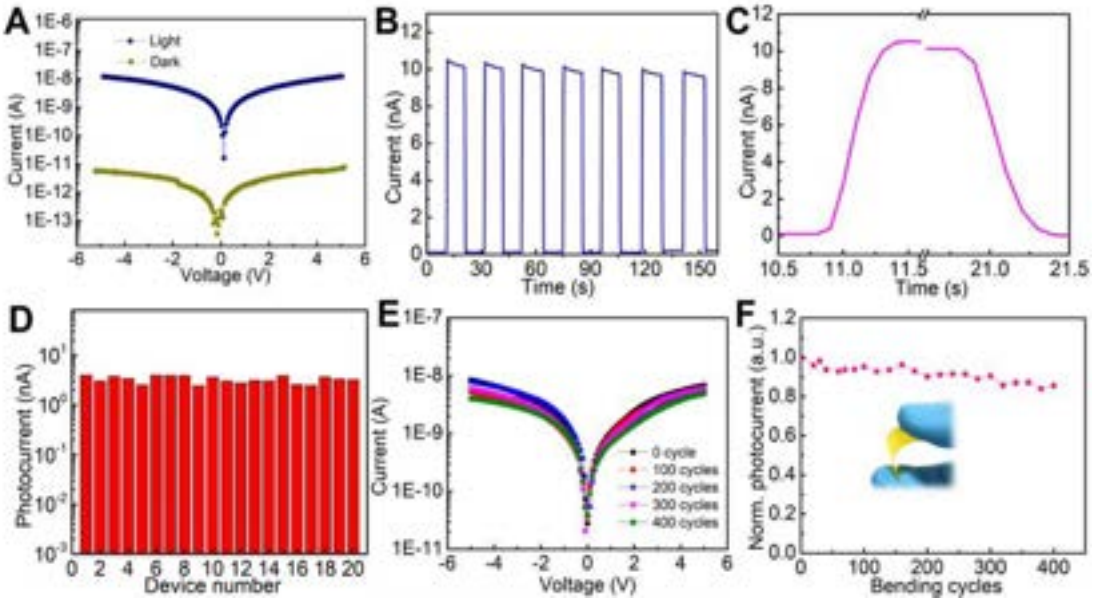

Figure 3. PbI_2 film-based photodetector performance: (**A**) I-V characteristics of PbI_2 thin film-based photodetector under dark and light conditions; (**B**) Typical photoresponse of the device obtained using 405 nm LED radiation with the power of 2 mW/cm^2 at a bias voltage of 5 V; (**C**) Fast device photoresponse, giving the rise time (~360 ms) and decay time (~380 ms), respectively; (**D**) Statistics of the measured photocurrent for 20 devices on the PbI_2 thin film; (**E**) The I-V curves of the flexible photodetector under light illumination without and after different bending times; and (**F**) Stability of the device after bending it 400 times. Inset: a photograph of the bending devices. The bending angle is around 45°.

Following our hypothesis of the film growth, PbI_2 thin films formed at the liquid-air interface can be ascribed to the relative fast descending liquid interface relative to the slow solute diffusion in the solution. In a typical process, solvent evaporation at 210 °C lowers the solution interface by ~2 mm over 60 minutes during the growth process. At the same time, the one-way characteristic diffusion length of PbI_2 along the vertical distance from liquid-air interface is ~2.1 mm based on $\sqrt{D_{avg}t}$,[41] where D_{avg} is the average diffusion coefficient for Pb^{2+} and I^- ions and $D_{avg} \approx 1285\ \mu m^2 s^{-1}$. It should be noted that the hydration effects on the ions (Pb^{2+} and I^-) are not considered and the ionic radii are used to estimate diffusivity. More details on the diffusivity calculation could be found in the experimental methods. Thus, the descending solution interface has a comparable speed to the diffusion process. PbI_2 tends to aggregate close to the interface leading to a concentration spike and precipitates at the liquid-air interface as solvent evaporates.

To demonstrate the potential of a controllable film growth, we introduce a simple analytical model considering the coupling of evaporation and diffusion. Due to the low solubility of PbI_2 in glycerol (Figure S14), a constant solute diffusivity can be assumed at

a constant temperature. Figure 4A displays the schematic illustration of the concentration profile along z direction normal to the bottom, and the initial bulk solution concentration is c_0. After a rapid evaporation time Δt, the interface descends with the height reduction, $\Delta h = R\Delta t$. A concentration spike occurs at the interface, where c_p represents the peak concentration at the interface, c^* is the critical concentration above which films can nucleate and grow inside the solution. Therefore, the length scale of film thickness (L^*) can be expressed as: $L^* = \frac{c_p - c^*}{c_p - c_0} L$, where L is the characteristic length for supersaturation region. Since the solute (PbI_2) does not evaporate at a low temperature, the mass balance equation for the solute in the evaporated layer (Δh) can be expressed as: $c_0 \Delta h = \frac{1}{2} L(c_p - c_0)$. Then, we can obtain the expression for the length scale of film thickness: $L^* = \frac{(c_p - c^*)}{2c_0} \cdot \frac{D}{R}$. More detailed derivation can be found in Supplementary Note 1. Considering the low solubility of PbI_2 in glycerol at different temperatures (Figure S14), the characteristic film thickness, L^*, scales linearly with a critical parameter, $\frac{D}{R}$. The dimensionless pre-factor, $\frac{(c_p - c^*)}{2c_0}$, reflects how much oversaturation is allowed in the system, which can be related to the nucleation rate and solvent evaporation. Therefore, film thickness can be well tuned through controlling solvent evaporation rates and diffusivity of solute. As shown in Figure 4B, fully covered PbI_2 films in a Φ 60 mm petri dish could be obtained at different temperatures from 180 °C to 220 °C. The calculated FWHM of the (001) XRD peak has similar values (Figure S15), indicating that single crystal quality of PbI_2 thin films could be obtained within a flexible temperature window. Meanwhile, solvent evaporation rates and solute diffusivity could be tailored by controlling temperature (Figure 4C), providing the flexibility in controlling the film thickness. This is shown by the increased transparency of the films (shown in Figure 4B), implying a continuous decrease of film thickness as temperature increases. The measured thicknesses of films synthesized at different solvent evaporation rates can be adjusted from sub-micrometer to several micrometers (Figure 4D). Interestingly, the reduction in film thicknesses with increased evaporation rates follows the same trend with the value of D/R. By fitting the measured film thickness with D/R, a clearly linear correlation is revealed with a slop value of 0.001 (Figure S16), demonstrating that the film thickness is highly correlated to the evaporation rate and solute diffusivity and could be well predicted by calculating the value of D/R.

To further validate the analytical model and the critical parameter in predicting film thickness, PbI_2 films are grown by controlling solvent evaporation rates at a constant temperature (*i.e.* 210 °C). The evaporation rate of solvent can be adjusted by varying the covering evaporation surface with glass slides, and a constant diffusivity of solute is assumed at the constant temperature. The obtained film thicknesses at different evaporation rates could be fitted well by a linear correlation (Figure 4E) as a function of D/R, confirming the validity of the analytical model in predicting the film thickness, $L^* = 0.001 \frac{D}{R}$. For our systems in which with a nucleation rate is much faster than the evaporation rate as inferred from MD simulations, only small amount of oversaturation is

required before precipitation occurs. Thus, the pre-factor, $\frac{(c_p - c^*)}{2c_0}$, should be much less than unity. For systems with a nucleation rate comparable to the evaporation rate, substantial oversaturation is possible such that the pre-factor, $\frac{(c_p - c^*)}{2c_0}$, will be much larger. Based on the prediction of the simple analytical model and the critical parameter, D/R, we synthesized a 122 nm thickness PbI_2 film by controlling solvent evaporation rate and solute diffusivity, as shown in Figure S17. As the evaporation rate and solute diffusivity can be controlled by multiple variables such as temperature, solvent viscosity and composition, we expect a wide range of flexibility in synthesizing large-area free-standing thin films with controlled film thicknesses even down to a few monolayers at the liquid-air interface under controlled evaporation conditions.

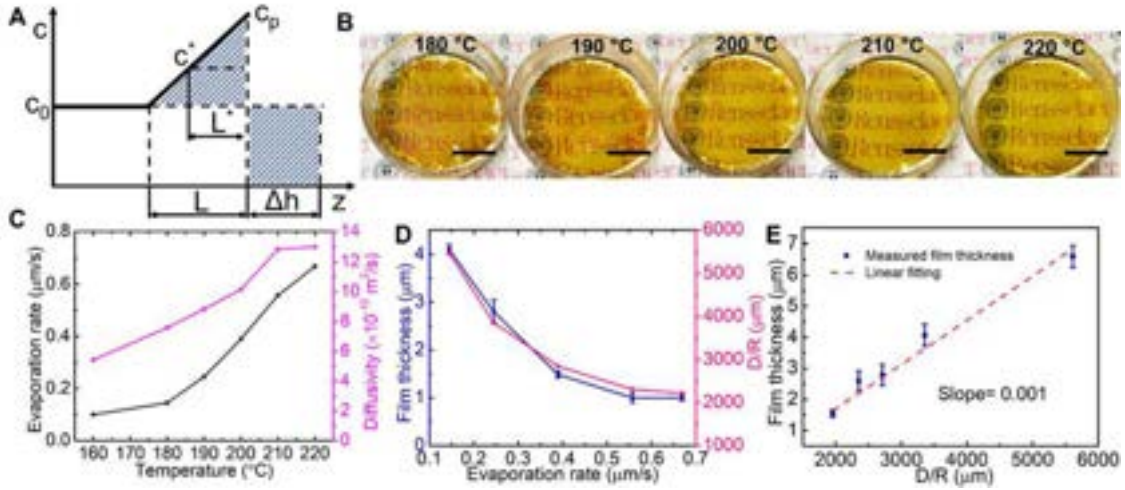

Figure 4. An analytical model and a critical parameter D/R enabling the prediction and control of PbI_2 film thicknesses. (**A**) A schematic profile of PbI_2 concentration along solution height (z) after evaporating solvent by a height of Δh; (**B**) Optical images of PbI_2 films obtained by tailoring solvent evaporation rate at different temperature. Scale bars: 2 cm; (**C**) The temperature dependence of the evaporation rate and diffusivity; (**D**) The film thickness and D/R change at different evaporation rates as controlled by different temperature; and (**E**) Evaporation rate-film thickness graph through varying flow rates at a constant temperature, 210 °C, with a linear fitting.

Molecular dynamics simulations[42] are performed to further reveal the mechanism and kinetics of film growth and obtain theoretical understanding in the relation between the film thickness and the evaporation rate. The details of the force field used to model PbI_2 and the model solvent can be found in the experimental methods and Supplementary Note 2. The MD simulation starts with ~30000 model PbI_2 molecules dispersed in about 45000 model solvent molecules, as shown in Figure 5A. A gas-liquid equilibrium for solvent has been established at the beginning of the simulation. Grand-Canonical Monte Carlo (GCMC) steps[43] have been introduced under a constant frequency to the top of the simulation box in order to remove the solvent gas, resulting in continuous evaporation of the solvent liquid. The evaporation rate can be adjusted by the frequency of the GCMC operation. The

evaporation simulation setup is illustrated in Figure S18. As the solvent evaporates, the solute left-behind starts to concentrate near the solution-gas interface, which can be seen on Figures 5A and B. The peak of Pb concentration increases, and the supersaturation region widens. Due to PbI_2 supersaturation, PbI_2 precipitates out as a layered structure near the solution-gas interface (Figure 5A, Movie S2). Upon further evaporation, a PbI_2 film grows and covers the entire solution-gas interface. Importantly, the evaporation rate reduces as the Pb and I particles must diffuse through the already-formed PbI_2 solid film, as seen in Figures 5C, D and E. Once the film fully covers the interface, evaporation becomes low, leading to self-termination of the precipitation process. This self-limiting growth is consistent with our experimental observation, as illustrated in Figure S19.

In addition, by tuning the evaporation rate, the film thickness can be well-controlled (Figure 5F). A faster evaporation rate tends to result in a thinner film thickness, while having smaller crystal-domains due to the rapid nucleation at the interface (Figure S20, Movies S2 and S3). As PbI_2 grows at the liquid/air interface, it increases the surface coverage along with decreasing the evaporation rate and increasing the film thickness (Figures 5C-E). It is found that a higher evaporation rate leads to a faster nucleation rate, indicating that the nucleation process is mainly controlled by diffusion process. As solvent evaporating, the concentrations of both Pb and I particles increase. Compared to the PbI_2 concentration, the diffusivities of Pb and I particles are more sensitive to the temperature (Figure S21). This suggests that the dominate factor to control film thickness is the solvent evaporation rate at a constant temperature. The measured film thickness follows an inverse function of R, and the fitting constant ($5.1 \times 10^{-10}\ m^2/s$) obtained is very close to diffusivity of Pb particles at 595 K ($4.8 \times 10^{-10}\ m^2/s$), as shown in Figure 5F and Figure S21B. This demonstrates again that we are able to predict the film thickness only by acquiring solvent evaporation rate and solute diffusivity. At different temperatures, the film thickness depends on the interplay among diffusivity and solvent evaporation rate as expressed by the critical parameter of D/R in the analytical model.

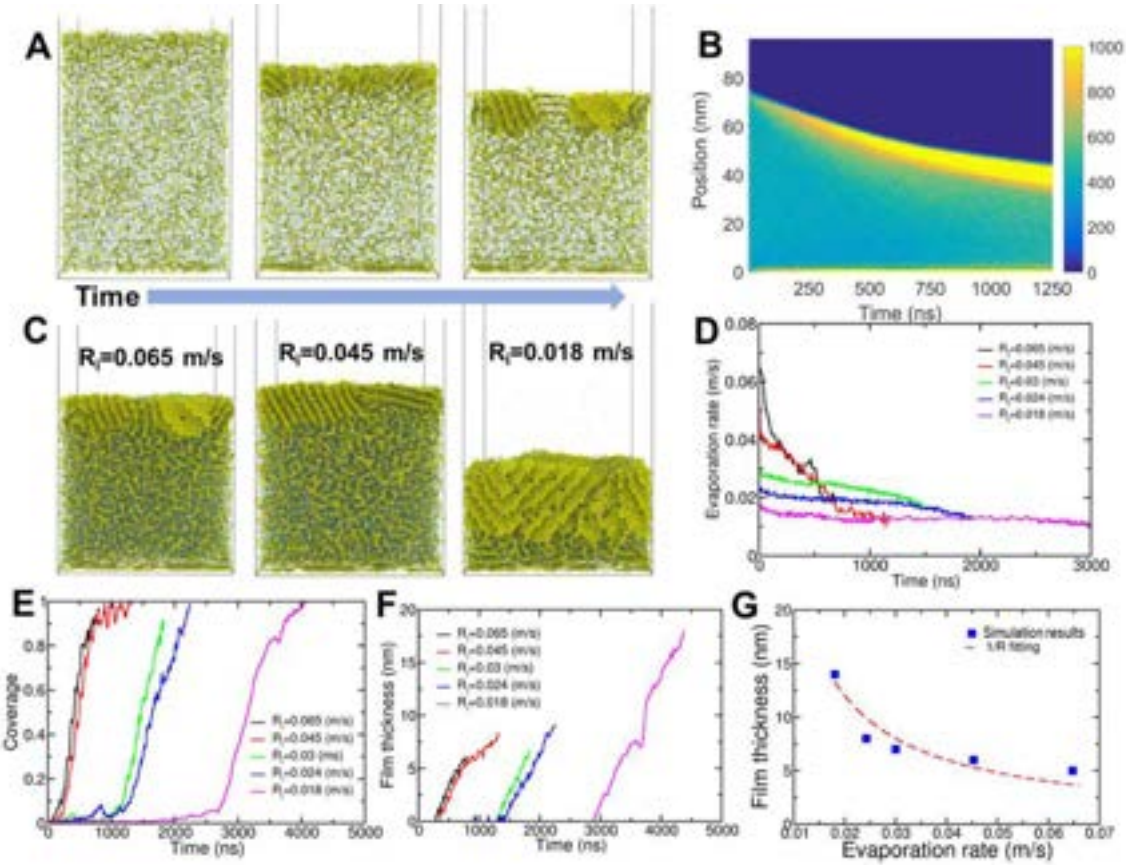

Figure 5. Molecular dynamics simulations of PbI_2 films growth at the liquid-air interface, revealing growth mechanisms and its kinetics: (**A**) Snapshots of PbI_2 solution within a 5-nm slice with an initial evaporation rate R=0.3 m/s and R=0.11 m/s; (**B**) The Pb concentration distribution (number of Pb particles in a volume of 288 nm^3) as a function of evaporation time. The initial evaporated rate is ~0.14 m/s; (**C**) The instantaneous evaporation rate as a function of time for different initial evaporation rate to up 90% of surface coverage; The film surface coverage (**D**) and thickness (**E**) as a function of time for different initial evaporation rates; (**F**) Film thickness at 90% surface coverage as a function of the initial evaporation rate. The red dash line is a fitting of the form 1/R.

The solvent-evaporation controlled method has been successfully demonstrated in growth of large-area free-standing PbI_2 thin film under a desirable solvent condition. Based on our MD simulation results, a concentration spike appears as fast solvent evaporates, resulting in thin film growth at the liquid-air interface. In addition, the film thickness can be well adjusted by tuning the solvent evaporation condition and solute diffusivity. Thus, we believe that large-area thin films for a wide range of material systems could be realized by designing an appropriate combination of solvent and evaporation conditions. We applied the solvent evaporation approach to grow large-area hybrid perovskite films. $MAPbI_3$ films could be grown at the liquid-air interface by evaporating a mixture of PbI_2 and methylamine in hydriodic acid solution at 100 °C (see details in the experimental methods). The obtained film has a uniform thickness with a well-defined film edge, suggesting good crystallinity of the $MAPbI_3$ film (Figure 6A). The XRD pattern also

confirms high crystallinity with preferential orientation along [001] direction. The measured FWHM of (004) diffraction peak is as small as 0.12° (Figure 6B), which is close to the reported values of $MAPbI_3$ single crystal films.[17,21] The evaporation rate can be controlled through varying evaporation areas similar as the previous reported method[21] such that the film thickness can be controlled from 40 μm down to a few microns, and the free-standing $MAPbI_3$ film can be directly transferred to fabricate optoelectronics or solar cell applications. The $MAPbI_3$ film thickness decreases as increased evaporation rates, following the trend of 1/R function by assuming a constant diffusivity at a constant temperature (Figure 6C). This further validates the feasibility of using the simple analytical model and the critical parameter of D/R in predicting the film thickness under the evaporation-controlled synthesis route.

In addition, $MAPbBr_3$ and BiI_3 with a preferential orientation along [00l] direction could also be obtained at the liquid-air interface with high crystallinity (Figures 6D-G). This method was further demonstrated on 2D perovskites, such as $(C_2H_9NH_3)_2PbI_4$ (BA_2PbI_4), $(C_4H_9NH_3)_2$ $(CH_3NH_3)Pb_2I_7$ ($BA_2MAPb_2I_7$), and $C_8H_9NH_3PbI_4$ (PEA_2PbI_4). As shown in Figures 6H-J, it displays a uniform thin film grown on the solution surface which fully covers a Φ 60 mm petri dish, suggesting that a larger thin film could be achieved by enlarging the size of the container. Figure 6K demonstrates good flexibility of the transferred PEA_2PbI_4 thin film on the PET substrate. The XRD measurements (Figures S22A-C) indicate that the highly oriented films can be obtained as well using the solvent evaporation method. To investigate the domain orientations, EBSD were performed. As shown in Figures S23A-F, the obtained BA_2PbI_4 film displays similar Kikuchi patterns at four different positions, indicating the same crystallographic orientation and no grain boundaries within the crystal. Figure S23F shows the crystallographic orientation mapping with a uniform color, indicating the crystal has a single orientation. The single orientation was confirmed by the inverse pole figure mapping, as shown in Figure S23G. For PEA_2PbI_4 perovskite, IPF mapping was conducted across the selected area in Figure S24A. The uniform color within IPF X, Y and Z mappings suggest the single orientation of the film (Figures S24B-E). Therefore, it demonstrates that the solvent evaporation method is a versatile method capable of fabricating uniaxial orientation growth of large area free-standing films across various material systems. Meanwhile, 3D heterostructures could also be realized, as shown in Figure S25. Using as-grown PbI_2 film as a substrate on BiI_3 solution surface, PbI_2/BiI_3 heterostructure can be obtained at the liquid-air interface. The SEM image of the obtained film shows an obvious 2-layer heterostructure (Figure S25A). Figure S25B displays a close look at the heterostructure, which exhibits a smooth and flat PbI_2 layer and a flake-flower BiI_3 layer. The flake-flower BiI_3 are growth vertically on the flat PbI_2 thin film. The vertical structure would be beneficial for the charge carrier transfer. Therefore, various complex 3D heterostructures could be expected. The ultimate control of the film dimension, film uniformity and quality depends on the interplay between materials intrinsic properties and the control of the evironmental variables as predicated by the solvent evaporation rates and solute diffusivity.

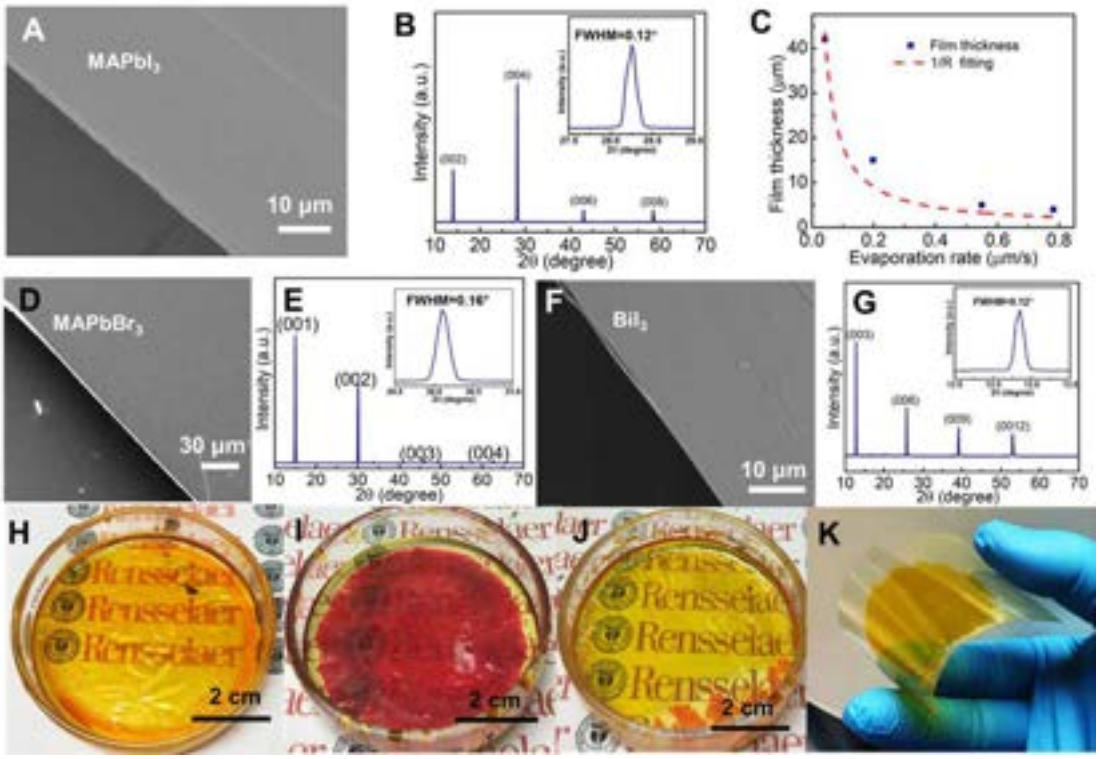

Figure 6. Perovskite thin films grown at the liquid-air interface: A SEM image (**A**) and XRD pattern (**B**) of a $MAPbI_3$ thin film; (**C**) Correlation between the large-area 2D $MAPbI_3$ film thickness and evaporation rate; A SEM image (**D**) and a XRD pattern (**E**) of the $MAPbBr_3$ thin film grown at the liquid-air interface; Optical images of free-standing (**H**) BA_2PbI_4, (**I**) $BA_2MAPb_2I_7$, and (**J**) PEA_2PbI_4 thin films grown on the solution surface by direct solvent evaporation; (**K**) An optical image of a PEA_2PbI_4 thin film transferred on a PET substrate, displaying good flexibility.

CONCLUSIONS

In summary, we demonstrate a versatile solution-based approach to synthesize large-scale freestanding uniaxial oriented thin films with millimeter sized grains at the liquid-air interface as driven by the supersaturation of solute during solvent evaporation. Grains nucleate and coalescence to form small islands, then grow laterally into large area uniform thin films. The quality of the obtained films is comparable to the single crystalline films, as confirmed by XRD measurements and optoelectronic performance. EBSD results demonstrate the single orientation within the film. A critical parameter (D/R) is discovered enabling the manipulation and prediction of the film thickness based on an analytical model and MD simulation, which is further validated by experiments. This evaporation-controlled approach can be adopted to fabricate across multiple material systems of metal halides and hybrid perovskites at the liquid-air interface. The lateral dimension of the thin films is only confined by the dimension of containers. Therefore, the solution-based approach is a potentially high-throughput and cost-effective approach that can be used to grow large

scale high quality thin films at the liquid-air interface across a wide range of material systems.

EXPERIMENTAL METHODS

Growth of single crystalline PbI_2 films. Typically, 5 mL of glycerol was added to the bottom of a petri dish (Φ 60 mm), followed by heating the solution on a hot plate at different temperature (160 °C ~ 220 °C) in the fume hood with constant air flow. ~1800 μL of PbI_2 solution (50 mg/mL in dimethylformamide, DMF) was carefully added to the solution. During the solvent evaporation, PbI_2 film was assembled at the liquid-air interface. After about 1 hour, a shiny free-standing yellow thin film can be obtained at the top of solution. Then, water was added into the petri dish to float the prepared film after the solution was cooled down. The free-standing PbI_2 film was then transferred to other substrates. The transferred film was then washed in ethanol and dried in a vacuum chamber at room temperature for further characterization. The flexibility of PbI_2 film can be affected by many factors, such as film thickness, substrate thickness, film patterning, additional protection layer, which needs further investigation. For larger-area growth of PbI_2 thin films, it only needs to expand the system using larger size of petri dishes.

Synthesis of PbI_2 wires. 10 mL ethylene glycol (EG) was added to a petri dish (Φ 60 mm). 2 mL of PbI_2 solution (80 mg/mL in DMF) was carefully added to EG by drops to form light yellow solution. Then the solution was heated at 160°C on the hot plate. As solvent evaporating, yellow wires were formed at the bottom of the petri dish. The obtained yellow wires were transferred on glass substrates for further characterization.

Synthesis of $MAPbI_3$ thin films. The method is similar as reported previously.[21] Typically, PbI_2 powder (1.4 g) was dissolved in 15 mL of hydriodic acid (HI, 57% w/w aq. solution) in a 50 mL beaker, following by adding 200 μL of methylamine solution (33 wt.% in absolute ethanol) and stirring to form a clear solution. Then, the solution was poured into a petri dish (Φ 60 mm) and heated on a hot plate at 100 °C. Two glass slides was placed on top of the petri dish to cover the solution. The film thickness was tuned by adjusting the gap of the two glass slides to change the solvent evaporation rate. The solution was evaporated until fully-coverage film was formed at the solution surface.

Synthesis of $MAPbBr_3$ thin films. Similarly, $PbBr_2$ (1.53 g) was dissolved in 15 mL of hydrobromic acid (HBr, 48% w/w in aq. solution) and 0.2 g of methylamine solution (33 wt.% in absolute ethanol) was added into the solution. The solution was heated in a petri dish on the hot plate at 90 °C until a thin film formed at the solution-air interface.

Synthesis of BiI_3 thin films. BiI_3 powder (700 mg) was added in pure glycerol (10 mL). The mixture was stirred and heated at 210 °C until a clear solution formed. Then, the solution was heated at the constant temperature to evaporate the solvent until BiI_3 film formed at the solution surface.

Synthesis of 2D perovskite thin films. The method is similar as discussed above. For BA_2PbI_4 or PEA_2PbI_4 perovskites, n-butylamine or 2-phenylethylamine mixed with PbI_2 (2:1), and dissolved in hydroiodic acid (5 mL). Then, the solution was added into a petri

dish and evaporated on a hot plate at 85 °C. In order to lower the nucleation rate, two glass slides were placed on the top of the petri dish and left a gap about 5 mm. For $BA_2MAPb_2I_7$ perovskite, the ratio between n-butylamine and methylamine are 2:1. Then, following the same steps to prepare the thin film. For the large thin film transfer, n-propanol was used as a solvent to float perovskite film on its surface. Then the perovskite film was transferred to the desire substrate by a lift-off method. The extra solvent can be washed out by toluene. The transferred film can be dried under vacuum.

Measurements and characterizations. The morphology was characterized with field emission scanning electron microscopy (FE-SEM) (Carl Zeiss Supra 55). The multi-position XRD measurements on the film were taken on the Panalytical X'Pert Diffractometer using 1° slit. If not specified, X-ray powder diffraction (XRD) and pole figure measurements were conducted to characterize the crystallinity and texture of PbI_2 thin films on Bruker D8-Discover (Germany). The crystal structures were visualized using VESTA.[44] Atomic force microscopy (AFM) images were recorded using a Digital Instruments Nanoscope IIIa MultiMode microscope. The UV-vis spectrum was measured in the range 300 – 800 nm by Perkin Elmer Lambda 950 UV spectrometer. The photoluminescence (PL) spectrum was performed on a Spex Fluorolog Tau-3 spectrofluorometer with a xenon lamp, and the excitation wavelength was fixed at 350 nm. Temperature dependent PL measurements were conducted using a customized PL system including a Picoquant 405 nm pulsed laser with a 2 mW power and a repetition of 4 MHz, a Thorlabs 4 Megapixel Monochrome Scientific CCD Camera, a Princeton Instruments SP-2358 spectrograph. Time resolved photoluminescence (TRPL) was measured in the same PL system. A Picoquant PDM series single-photon detector synchronized with the pulsed laser source was used to collect the time domain PL information. The film thickness was measured by a surface profiler (Dektak 6M, Veeco).

Device fabrication and optoelectronic property measurements. For the device fabrication, the PbI_2 thin film was firstly transferred onto a PET substrate by a lift-off method from water surface. The substrate with PbI_2 film was washed by ethanol several times and dried in a vacuum chamber. A copper grid was used as the shadow mask and attached onto the substrate to afford a channel width of 80 μm and length of 40 μm. Au (50 nm) thin film was deposited using electron beam evaporation as the electrical contact electrodes. The photoelectronical measurements were performed on a Keithley 4200 probe station. A LED of 405 nm was used as the light source with the incident power of 2 mW/cm^2 for the photodetector measurements. The responsivity (R) is defined as the photocurrent generated per unit power of light incidence on the effective area, which can be calculated by the following equation:[45,46]

$$R = \frac{I_p}{PS} \quad (1)$$

where I_p is the photocurrent, P is the light intensity, and S is the active area of the photodetector. The Detectivity (D^*) reflects the photodetector's sensitivity, as expressed[45,46]:

$$D^* = R\sqrt{\frac{S}{2eI_d}} \quad (2)$$

where e is the absolute value of the charge of an electron, and I_d is the dark current.

Solubility measurements. The procedure of measuring solubility of PbI_2 in glycerol at different temperature included adding PbI_2 powder in pure glycerol and heated on a hotplate at a constant temperature until PbI_2 was fully dissolved. Then, more PbI_2 powders were added into the solution until the equilibrium was reached. The saturation was confirmed by observation of the presence of undissolved solute and re-dissolving after a small amount of glycerol addition. The PbI_2 concentration was then determined by measuring the total amount of PbI_2 added into solvent.

Diffusion coefficients. We determined the diffusion coefficients (diffusivity), D, for individual salt ions using the Stokes-Einstein relation as follows:[41,47]

$$D = \frac{k_B T}{6\pi\eta r} \quad (3)$$

where k_B is Boltzmann's constant, T is the temperature, η represents the viscosity of solvent, and r is the hydrodynamic radius. It is noted that the hydration effects on the ions (Pb^{2+} and I^-) was not included and the ionic radius was used to estimate diffusivity. Due to the small amount of PbI_2 (~90 mg) in glycerol solvent (>3 g), we determined the solution viscosity only based on pure glycerol solvent. The solvent viscosity could be calculated by the formula proposed from previous report.[48] Then, the average diffusivity of the PbI_2 was estimated by the equation as expressed[49,50]:

$$D_{avg} = \frac{|Z_1|+|Z_2|}{(|Z_2|/D_1+|Z_1|/D_2)} \quad (4)$$

where D_{avg} is the overall diffusion coefficient for the salt in solution, Z_i is the cation/anion charge, and D_i is the cation/anion diffusion coefficient in solution.

Molecular dynamics simulations of PbI_2 film growth. Classical molecular dynamic simulations were carried out in LAMMPS package[43] using the force field described above. The visualization software OVITO[51] was used to generate simulation snapshots, animations. The equations of motion were integrated by Velocity-Verlet algorithm with a time step of 0.005 in reduced unit. Nose-Hoover thermostat were used to control the temperature of the system.[52,53] The unit conversion is followed a procedure in previous paper.[54] The size of simulation box is ~47 nm (X) × 24 nm (Y) × 24 nm (Z). Periodic boundary condition is applied in Y and Z dimensions. There are two walls capping at the two ends in the X-direction, each interacting with all particles following Lennard-Jones 9-3 form. The sample is illustrated in Figure S18.There are 30000 PbI_2 molecules 45000 solvent particles (equal amount of S_A and S_B particles). We select the number density and temperature such that the solvent particles form a mixture of liquid and gas, while the liquid solvent contains the solute PbI_2 (PbI_2 does not evaporate into the gas phase). The solute concentration is ~40%. The solution is in equilibrium at 595 K. The solubility limit is about 70% at this temperature. Note that there is a very small force to the left (11.7 *fN*) acting on

all particles (very much like gravity) such that the liquid phase is on the left of the system as shown in Figure S18. The evaporation process is accomplished by couple grand canonical Monte Carlo (GCMC) operations[43] with the MD simulation. GCMC operations are conducted at well controlled frequency (from ~0.2 to 2 ps^{-1}) over a region that ~1 nm thick near the top of the simulation box to control the evaporation rate. As evaporate continues, the liquid-gas interface moves which induces oversaturation of PbI_2 solutes and precipitation as shown in Movies S2 and S3. Please note that the evaporation process is not directly affected by the GCMC operations, such that the evaporation rate is generally not a constant (as can be seen in Figure 4C). The projection images were obtained by capturing snapshots along X direction when the film coverage reaches 90% at the interface.

The diffusivity of Pb and I atoms is obtained by calculating from mean-squared displacement ($\text{MSD} = [r_i(t) - r_i(0)]^2$), and using the long time limit of Einstein relation:[55]

$$D = \frac{[r_i(t) - r_i(0)]^2}{6t} \quad (9)$$

where $r_i(t)$ is the position of the atom i at time t.

ASSOCIATED CONTENT

Supporting Information

The derivation of Characteristic length of film thickness (L^*), MD simulation method, Optical images of PbI_2 film growth process, SEM images of PbI_2 grain coalescence, AFM images of the growth steps on the PbI_2 film, UV-Vis spectrum and PL measurement, Table of PbI_2 based photodetectors, PbI_2 solubility, XRD of PbI_2 films synthesized at different temperature, AFM of thin PbI_2 film, MD simulation results at different evaporation rates, XRD results of various perovskites.

Movie of PbI_2 film grown at the liquid-air interface, Movies of PbI_2 film growth at the liquid-air interface using MD simulation.

AUTHOR INFORMATION

Corresponding Author

* lianj@rpi.edu (J. Lian)

ORCID

Weiguang Zhu: 0000-0003-0007-9284

Yunfeng Shi: 0000-0003-1700-6049

Mingxin Li: 0000-0003-3276-9140

Jie Lian: 0000-0002-9060-8831

Author Contributions

The scope of the experiment was designed by W. Z. and J. L. W.Z., S.C. and J. S. carried out the material synthesis, and materials characterizations. W.Z performed pole figure measurements. W.Z., J. S. and M. L. fabricated the flexible photodetectors. W. Z. conducted the optical property measurements and evaluated the optoelectronic performance of photodetector. Y. Z. and Y. S. conducted the mechanism study of thin film growth process using molecular dynamics simulation and performed simulation data analyses. W.Z. and J. L. wrote the manuscript. All the authors helped on the paper editing.

ACKNOWLDGEMENTS

The work was supported as part of the Center for Performance and Design of Nuclear Waste Forms and Containers, an Energy Frontier Research Center funded by the U.S. Department of Energy, Office of Science, Basic Energy Sciences under Award # DE-SC0016584. J. L. also acknowledged the support of the US National Science Foundation under a grant the award of DMR 1742806. Y. Zhang and Y. Shi were supported by the National Science Foundation under Grants DMR-1508410. The simulations were carried out in the Center for Computational Innovations (CCI) at Rensselaer.

COMPETING INTERESTS

The authors declare no competing financial interests.

DATA AND MATERIALS AVAILABILITY

All data generated/need to evaluate the conclusion for the current study are available from the corresponding author on reasonable request.

REFERENCES

(1) Singh, J. *Electronic and Optoelectronic Properties of Semiconductor Structures*; Cambridge University Press, 2007.

(2) Liu, Y.; Yang, Z.; Cui, D.; Ren, X.; Sun, J.; Liu, X.; Zhang, J.; Wei, Q.; Fan, H.; Yu, F. Two-Inch-Sized Perovskite $Ch_3nh_3pbx_3$ (X= Cl, Br, I) Crystals: Growth and Characterization. *Adv. Mater.* 2015, *27*, 5176.

(3) Shi, D.; Adinolfi, V.; Comin, R.; Yuan, M.; Alarousu, E.; Buin, A.; Chen, Y.; Hoogland, S.; Rothenberger, A.; Katsiev, K. Low Trap-State Density and Long Carrier Diffusion in Organolead Trihalide Perovskite Single Crystals. *Science* 2015, *347*, 519.

(4) Dong, Q.; Fang, Y.; Shao, Y.; Mulligan, P.; Qiu, J.; Cao, L.; Huang, J. Electron-Hole Diffusion Lengths >175 Mm in Solution-Grown $Ch_3nh_3pbi_3$ Single Crystals. *Science* 2015, *347*, 967.

(5) Saidaminov, M. I.; Abdelhady, A. L.; Murali, B.; Alarousu, E.; Burlakov, V. M.; Peng, W.; Dursun, I.; Wang, L.; He, Y.; Maculan, G. High-Quality Bulk Hybrid Perovskite Single Crystals within Minutes by Inverse Temperature Crystallization. *Nat. Commun.* 2015, *6*, 1.

(6) Wang, Q.; Chen, B.; Liu, Y.; Deng, Y.; Bai, Y.; Dong, Q.; Huang, J. Scaling Behavior of Moisture-Induced Grain Degradation in Polycrystalline Hybrid Perovskite Thin Films. *Energy Environ. Sci.* 2017, *10*, 516.

(7) Leguy, A. M.; Hu, Y.; Campoy-Quiles, M.; Alonso, M. I.; Weber, O. J.; Azarhoosh, P.; Van Schilfgaarde, M.; Weller, M. T.; Bein, T.; Nelson, J. Reversible Hydration of $Ch_3nh_3pbi_3$ in Films, Single Crystals, and Solar Cells. *Chem. Mater.* 2015, *27*, 3397.

(8) Zhu, X.; Yang, D.; Yang, R.; Yang, B.; Yang, Z.; Ren, X.; Zhang, J.; Niu, J.; Feng, J.; Liu, S. F. Superior Stability for Perovskite Solar Cells with 20% Efficiency Using Vacuum Co-Evaporation. *Nanoscale* 2017, *9*, 12316.
(9) Ávila, J.; Momblona, C.; Boix, P. P.; Sessolo, M.; Bolink, H. J. Vapor-Deposited Perovskites: The Route to High-Performance Solar Cell Production? *Joule* 2017, *1*, 431.
(10) Wang, Y.; Sun, X.; Chen, Z.; Sun, Y. Y.; Zhang, S.; Lu, T. M.; Wertz, E.; Shi, J. High‐Temperature Ionic Epitaxy of Halide Perovskite Thin Film and the Hidden Carrier Dynamics. *Adv. Mater.* 2017, *29*, 1702643.
(11) Lau, C. F. J.; Deng, X.; Ma, Q.; Zheng, J.; Yun, J. S.; Green, M. A.; Huang, S.; Ho-Baillie, A. W. Cspbibr$_2$ Perovskite Solar Cell by Spray-Assisted Deposition. *ACS Energy Lett.* 2016, *1*, 573.
(12) Barrows, A. T.; Pearson, A. J.; Kwak, C. K.; Dunbar, A. D.; Buckley, A. R.; Lidzey, D. G. Efficient Planar Heterojunction Mixed-Halide Perovskite Solar Cells Deposited Via Spray-Deposition. *Energy Environ. Sci.* 2014, *7*, 2944.
(13) Yang, Z.; Chueh, C. C.; Zuo, F.; Kim, J. H.; Liang, P. W.; Jen, A. K. Y. High‐Performance Fully Printable Perovskite Solar Cells Via Blade‐Coating Technique under the Ambient Condition. *Adv. Energy Mater.* 2015, *5*, 1500328.
(14) Vak, D.; Hwang, K.; Faulks, A.; Jung, Y. S.; Clark, N.; Kim, D. Y.; Wilson, G. J.; Watkins, S. E. 3d Printer Based Slot‐Die Coater as a Lab‐to‐Fab Translation Tool for Solution‐Processed Solar Cells. *Adv. Energy Mater.* 2015, *5*, 1401539.
(15) Yang, Z.; Deng, Y.; Zhang, X.; Wang, S.; Chen, H.; Yang, S.; Khurgin, J.; Fang, N. X.; Zhang, X.; Ma, R. High‐Performance Single‐Crystalline Perovskite Thin‐Film Photodetector. *Adv. Mater.* 2018, *30*, 1704333.
(16) Chen, Y.-X.; Ge, Q.-Q.; Shi, Y.; Liu, J.; Xue, D.-J.; Ma, J.-Y.; Ding, J.; Yan, H.-J.; Hu, J.-S.; Wan, L.-J. General Space-Confined on-Substrate Fabrication of Thickness-Adjustable Hybrid Perovskite Single-Crystalline Thin Films. *J. Am. Chem. Soc.* 2016, *138*, 16196.
(17) Liu, Y.; Zhang, Y.; Yang, Z.; Yang, D.; Ren, X.; Pang, L.; Liu, S. Thinness‐and Shape‐Controlled Growth for Ultrathin Single‐Crystalline Perovskite Wafers for Mass Production of Superior Photoelectronic Devices. *Adv. Mater.* 2016, *28*, 9204.
(18) Chen, Z.; Dong, Q.; Liu, Y.; Bao, C.; Fang, Y.; Lin, Y.; Tang, S.; Wang, Q.; Xiao, X.; Bai, Y. Thin Single Crystal Perovskite Solar Cells to Harvest Below-Bandgap Light Absorption. *Nat. Commun.* 2017, *8*, 1.
(19) Zhumekenov, A. A.; Burlakov, V. M.; Saidaminov, M. I.; Alofi, A.; Haque, M. A.; Turedi, B.; Davaasuren, B.; Dursun, I.; Cho, N.; El-Zohry, A. M. The Role of Surface Tension in the Crystallization of Metal Halide Perovskites. *ACS Energy Lett.* 2017, *2*, 1782.
(20) Wang, K.; Wu, C.; Yang, D.; Jiang, Y.; Priya, S. Quasi-Two-Dimensional Halide Perovskite Single Crystal Photodetector. *ACS Nano* 2018, *12*, 4919.
(21) Liu, Y.; Dong, Q.; Fang, Y.; Lin, Y.; Deng, Y.; Huang, J. Fast Growth of Thin Mapbi$_3$ Crystal Wafers on Aqueous Solution Surface for Efficient Lateral‐Structure Perovskite Solar Cells. *Adv. Funct. Mater.* 2019, *29*, 1807707.
(22) Lee, J.-H.; Lee, E. K.; Joo, W.-J.; Jang, Y.; Kim, B.-S.; Lim, J. Y.; Choi, S.-H.; Ahn, S. J.; Ahn, J. R.; Park, M.-H. Wafer-Scale Growth of Single-Crystal Monolayer Graphene on Reusable Hydrogen-Terminated Germanium. *Science* 2014, *344*, 286.
(23) Lee, J. S.; Choi, S. H.; Yun, S. J.; Kim, Y. I.; Boandoh, S.; Park, J.-H.; Shin, B. G.; Ko, H.; Lee, S. H.; Kim, Y.-M. Wafer-Scale Single-Crystal Hexagonal Boron Nitride Film Via Self-Collimated Grain Formation. *Science* 2018, *362*, 817.

(24) Chen, T.-A.; Chuu, C.-P.; Tseng, C.-C.; Wen, C.-K.; Wong, H.-S. P.; Pan, S.; Li, R.; Chao, T.-A.; Chueh, W.-C.; Zhang, Y. Wafer-Scale Single-Crystal Hexagonal Boron Nitride Monolayers on Cu (111). *Nature* 2020, *579*, 219.
(25) Fu, D.; Zhao, X.; Zhang, Y.-Y.; Li, L.; Xu, H.; Jang, A.-R.; Yoon, S. I.; Song, P.; Poh, S. M.; Ren, T. Molecular Beam Epitaxy of Highly Crystalline Monolayer Molybdenum Disulfide on Hexagonal Boron Nitride. *J. Am. Chem. Soc.* 2017, *139*, 9392.
(26) Xu, X.; Zhang, Z.; Dong, J.; Yi, D.; Niu, J.; Wu, M.; Lin, L.; Yin, R.; Li, M.; Zhou, J. Ultrafast Epitaxial Growth of Metre-Sized Single-Crystal Graphene on Industrial Cu Foil. *Science bulletin* 2017, *62*, 1074.
(27) Vesselinov, M. I. *Crystal Growth for Beginners: Fundamentals of Nucleation, Crystal Growth and Epitaxy*; World scientific, 2016.
(28) Cubillas, P.; Anderson, M. W. Synthesis Mechanism: Crystal Growth and Nucleation. *Zeolites and catalysis: synthesis, reactions and applications* 2010, 1.
(29) Ishihara, T.; Goto, T. Large Optical Nonlinearity Due to Exciton State in Pbi_2. *J. Phys. Soc. Jpn.* 1988, *57*, 2191.
(30) Rybak, O.; Blonskii, I.; Bilyi, Y. M.; Lun, Y.; Makowska-Janusik, M.; Kasperczyk, J.; Berdowski, J.; Kityk, I.; Sahraoui, B. Luminescent Spectra of Pbi_2 Single Crystals Doped by 3d-Metal Impurities. *J. Lumin.* 1998, *79*, 257.
(31) Sun, H.; Zhao, B.; Yang, D.; Wangyang, P.; Gao, X.; Zhu, X. Flexible X-Ray Detector Based on Sliced Lead Iodide Crystal. *Phys. Status Solidi Rapid Res. Lett.* 2017, *11*, 1600397.
(32) Zhu, X.; Wei, Z.; Jin, Y.; Xiang, A. Growth and Characterization of a Pbi_2 Single Crystal Used for Gamma Ray Detectors. *Cryst. Res. Technol.* 2007, *42*, 456.
(33) Zentai, G.; Schieber, M.; Partain, L.; Pavlyuchkova, R.; Proano, C. Large Area Mercuric Iodide and Lead Iodide X-Ray Detectors for Medical and Non-Destructive Industrial Imaging. *J. Cryst. Growth* 2005, *275*, e1327.
(34) Zheng, W.; Zhang, Z.; Lin, R.; Xu, K.; He, J.; Huang, F. High-Crystalline 2d Layered Pbi_2 with Ultrasmooth Surface: Liquid-Phase Synthesis and Application of High-Speed Photon Detection. *Adv. Electron. Mater.* 2016, *2*, 1600291.
(35) Zhang, J.; Song, T.; Zhang, Z.; Ding, K.; Huang, F.; Sun, B. Layered Ultrathin Pbi_2 Single Crystals for High Sensitivity Flexible Photodetectors. *J. Mater. Chem. C* 2015, *3*, 4402.
(36) Wei, Q.; Shen, B.; Chen, Y.; Xu, B.; Xia, Y.; Yin, J.; Liu, Z. Large-Sized Pbi_2 Single Crystal Grown by Co-Solvent Method for Visible-Light Photo-Detector Application. *Mater. Lett.* 2017, *193*, 101.
(37) Lan, C.; Dong, R.; Zhou, Z.; Shu, L.; Li, D.; Yip, S.; Ho, J. C. Large-Scale Synthesis of Freestanding Layer-Structured Pbi_2 and $Mapbi_3$ Nanosheets for High-Performance Photodetection. *Adv. Mater.* 2017, *29*, 1702759.
(38) O'donnell, K.; Chen, X. Temperature Dependence of Semiconductor Band Gaps. *Applied physics letters* 1991, *58*, 2924.
(39) Woo, H. C.; Choi, J. W.; Shin, J.; Chin, S.-H.; Ann, M. H.; Lee, C.-L. Temperature-Dependent Photoluminescence of Ch3nh3pbbr3 Perovskite Quantum Dots and Bulk Counterparts. *The journal of physical chemistry letters* 2018, *9*, 4066.
(40) Liu, X.; Ha, S. T.; Zhang, Q.; de la Mata, M.; Magen, C.; Arbiol, J.; Sum, T. C.; Xiong, Q. Whispering Gallery Mode Lasing from Hexagonal Shaped Layered Lead Iodide Crystals. *ACS Nano* 2015, *9*, 687.
(41) Bigioni, T. P.; Lin, X.-M.; Nguyen, T. T.; Corwin, E. I.; Witten, T. A.; Jaeger, H. M. Kinetically Driven Self Assembly of Highly Ordered Nanoparticle Monolayers. *Nat. Mater.* 2006, *5*, 265.
(42) Zhang, Y.; Huang, L.; Shi, Y. Silica Glass Toughened by Consolidation of Glassy Nanoparticles. *Nano Lett.* 2019, *19*, 5222.

(43) Plimpton, S. *Fast Parallel Algorithms for Short-Range Molecular Dynamics*, Sandia National Labs., Albuquerque, NM (United States), 1993.
(44) Momma, K.; Izumi, F. Vesta: A Three-Dimensional Visualization System for Electronic and Structural Analysis. *J. Appl. Crystallogr.* 2008, *41*, 653.
(45) Han, M.; Sun, J.; Bian, L.; Wang, Z.; Zhang, L.; Yin, Y.; Gao, Z.; Li, F.; Xin, Q.; He, L. Two-Step Vapor Deposition of Self-Catalyzed Large-Size Pbi_2 Nanobelts for High-Performance Photodetectors. *J. Mater. Chem. C* 2018, *6*, 5746.
(46) Wang, R.; Li, S.; Wang, P.; Xiu, J.; Wei, G.; Sun, M.; Li, Z.; Liu, Y.; Zhong, M. Pbi_2 Nanosheets for Photodetectors Via the Facile Cooling Thermal Supersaturation Solution Method. *J. Phys. Chem. C* 2019, *123*, 9609.
(47) Miller, C. C. The Stokes-Einstein Law for Diffusion in Solution. *Proc. R. Soc. Lond. Series A, Containing Papers of a Mathematical and Physical Character* 1924, *106*, 724.
(48) Ferreira, A. G.; Egas, A. P.; Fonseca, I. M.; Costa, A. C.; Abreu, D. C.; Lobo, L. Q. The Viscosity of Glycerol. *J. Chem. Thermodyn* 2017, *113*, 162.
(49) Cussler, E. L. *Diffusion: Mass Transfer in Fluid Systems*; Cambridge university press, 2009.
(50) Tan, C. H.; Ng, H. Y. Modified Models to Predict Flux Behavior in Forward Osmosis in Consideration of External and Internal Concentration Polarizations. *J. Membr. Sci.* 2008, *324*, 209.
(51) Stukowski, A. Visualization and Analysis of Atomistic Simulation Data with Ovito–the Open Visualization Tool. *Modell. Simul. Mater. Sci. Eng.* 2009, *18*, 015012.
(52) Nosé, S. A Unified Formulation of the Constant Temperature Molecular Dynamics Methods. *J. Chem. Phys.* 1984, *81*, 511.
(53) Nosé, S. A Molecular Dynamics Method for Simulations in the Canonical Ensemble. *Mol. Phys.* 1984, *52*, 255.
(54) Sundararaman, S.; Huang, L.; Ispas, S.; Kob, W. New Optimization Scheme to Obtain Interaction Potentials for Oxide Glasses. *J. Chem. Phys.* 2018, *148*, 194504.
(55) Aryal, D.; Ganesan, V. Diffusivity of Mono-and Divalent Salts and Water in Polyelectrolyte Desalination Membranes. *J. Phys. Chem. B* 2018, *122*, 8098.

Table of Content